*Article*

# Effect of V on the Precipitation Behavior of Ti−Mo Microalloyed High-Strength Steel

Ruyang Han [1], Gengwei Yang [1,*], Deming Xu [1,*], Lu Jiang [2], Zhixiang Fu [1] and Gang Zhao [1]

1   The State Key Laboratory of Refractories and Metallurgy, Wuhan University of Science and Technology, Wuhan 430081, China
2   Institute for Frontier Materials Geelong, Deakin University, Waurn Ponds, VIC 3216, Australia
*   Correspondence: yanggengwei@126.com (G.Y.); xudeming@wust.edu.cn (D.X.);

**Abstract:** In this work, the precipitates in Ti−Mo−V steel were systematically characterized by high-resolution transmission electron microscopy (HRTEM). The thermodynamics and kinetics of precipitates in Ti−Mo and Ti−Mo−V steels were theoretically analyzed, and the effect of vanadium on the precipitation behavior was clarified. The results showed that the precipitation volume fraction of the Ti−Mo−V steel was significantly higher than that of Ti−Mo steel. The randomly dispersed precipitation and interphase precipitation (Ti, Mo, V)C particles coexisted in the Ti−Mo−V steel. When the temperature was higher than 872 °C, the addition of vanadium could increase the driving force for (Ti, Mo, V)C precipitation in austenite, resulting in an increased nucleation rate and shortened incubation period, promoting the (Ti, Mo, V)C precipitation. When the temperature was lower than 872 °C, the driving force for (Ti, Mo, V)C precipitation in austenite was lower than that for (Ti, Mo)C precipitation, and the incubation period of (Ti, Mo, V)C precipitation was increased. Moreover, it was also found that the precipitated-time-temperature curve of (Ti, Mo, V)C precipitated in the ferrite region was "C" shaped, but that of (Ti, Mo)C was "ε" shaped, and the incubation period of (Ti, Mo, V)C was significantly shorter than that of (Ti, Mo)C.

**Keywords:** high-strength ferritic steel; Ti−Mo−V complex microalloying; thermodynamics of precipitation; kinetics for precipitation; precipitation behavior

## 1. Introduction

With the development of industry, microalloyed high-strength steels have been widely used in transportation, automobile, construction, bridge and other engineering applications due to their excellent mechanical properties [1,2]. Microalloy and carbon atoms form nano-sized particles, which effectively hinder the movement of dislocations, thereby improving the strength of hot-rolled ferritic steels [3–5]. Among them, (Ti, Mo)C particles have a smaller size and higher coarsening resistance. Therefore, it is generally believed that Ti−Mo composite microalloying is more obvious to improve the properties of hot-rolled ferritic steels [6–8]. For instance, Funakawa et al. [9] indicated that the contribution of (Ti, Mo)C particles to yield strength was estimated to be over 300 MPa, and the yield strength of steel was significantly improved.

Recently, the literature [10–16] reported that adding Nb or V to Ti−Mo steel could further optimize microstructures and improve mechanical properties. Cai et al. [10] improved the yield strength of ultra-low carbon Ti−Mo steel to 680 MPa by adding Nb. Bu et al. [11] reported that the interphase precipitation in Ti−Mo−Nb steel could provide precipitation strengthening of ~320 MPa, resulting in its yield strength up to 747 MPa. Furthermore, our previous studies [12,13] also indicated that the addition of Nb on Ti−Mo hot-rolled ferritic steels could increase the contribution of precipitation strengthening. Meanwhile, the addition of Nb could also refine ferrite grains and inhibit bainitic transformation, thus improving the mechanical properties of hot-rolled ferritic steel. Compared to Nb, V could also

inhibit bainitic transformation and has a stronger ability for precipitation strengthening [14]. Zhang et al. [15] reported that Ti−Mo−V composite microalloying could improve the yield strength of ferritic steel to 900 MPa due to the contribution of nano-sized (Ti, Mo, V)C particles. Fu et al. [16] found that the contribution of precipitation strengthening provided by a large number of nano-sized spherical (Ti, Mo, V)C particles was up to ~40% of the yield strength in ferritic steel. In conclusion, the precipitation strengthening provided by nano-sized (Ti, Mo, V)C particles is a key factor to further improve the strength of the Ti−Mo−V steel. However, the previous studies [10–16] of Ti−Mo−V steel mainly focused on phase the microstructure and mechanical properties. The precipitation mechanism of (Ti, Mo, V)C particles and the effect of V addition on precipitation behavior has not been studied systematically yet. An in-depth study is needed. This is the innovation of this paper.

Therefore, based on the previous work, this paper further provides the quantitative of precipitation in Ti−Mo and Ti−Mo−V steels by means of electrolytically extracted phase analysis, and the effect of V addition on the precipitation behavior was clarified through theoretical analyses. The results will provide a theoretical basis for the development and production of Ti−Mo−V high-strength steels.

## 2. Materials and Experimental Procedure

The chemical compositions of the experimental steels are presented in Table 1. In total, 50 kg ingots were melted in a vacuum melting furnace and then forged into 250 mm × 100 mm × 60 mm billets. As shown in Figure 1, the billets were austenitized and homogenized at 1250 °C for 2 h and then hot-rolled to 3 mm in thickness via 7 passes with the finish rolling temperature of 860 °C. Subsequently, the hot-rolled sheets were cooled to 600 °C and held for 2 h to simulate the coiling process, followed by furnace cooling to ambient temperature.

**Table 1.** Chemical compositions of experimental steels (wt.%).

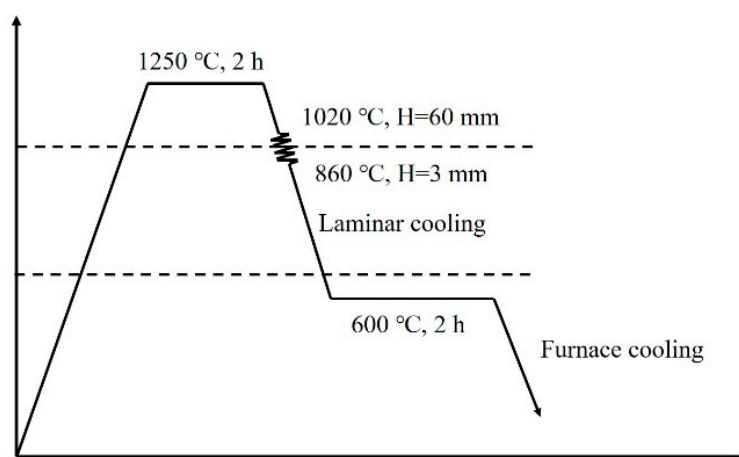| Steel | C | Si | Mn | Ti | Mo | V | Cr | N | Fe |
|-------|------|------|------|-------|------|------|------|--------|------|
| Ti−Mo | 0.06 | 0.07 | 1.44 | 0.097 | 0.28 | - | 0.21 | 0.0035 | Bal. |
| Ti−Mo−V | 0.08 | 0.14 | 1.48 | 0.10 | 0.30 | 0.24 | 0.22 | 0.0049 | Bal. |



**Figure 1.** Schematic diagram of rolling process.

The morphology and size of precipitates were characterized by a JEM-2100 transmission electron microscope (TEM) equipped with an energy dispersive spectroscope (EDS). The TEM samples were polished to less than 50 μm and punched into 3 mm discs. The discs were twin-jet polished with an electrolyte solution containing 6% perchloric acid and 94% ethyl alcohol. Subsequently, direction of the incident electron beam was adjusted parallel to the axis of the interphase precipitates band to observe the morphology of the

interphase precipitates. Meanwhile, more than 800 precipitated particles were measured in the TEM images to obtain the average particle size and distribution. In addition, the mass fraction of precipitates was determined by electrolytically extracted phase analysis, and the test procedure was described in the reference [17].

The meanings and units of symbols in the thermodynamic and kinetic model are shown in Table 2.

**Table 2.** Meanings and units of different symbols.

| Symbol | Meaning | Unit |
|--------|---------|------|
| $M_i$ | Amount of microalloyed element in the steel | wt.% |
| $[M_i]$ | Amount of solid solution of element $M_i$ | wt% |
| $f_v$ | Volume fraction of precipitation | % |
| $\rho_{Fe}, \rho_{MC}$ | Density of Fe and MC precipitated particles | kg/m$^3$ |
| $K$ | Temperature-independent constant | - |
| $t_{0da}$ | Temperature-independent parameter | s |
| $t_{0.05da}$ | Start time of precipitation that corresponds to the fraction precipitates 5% | s |
| $d^*$ | Size of critical nucleus in austenite | nm |
| $d_d{}^*$ | Size of critical nucleus in ferrite | nm |
| $A$ | Core energy of an edge dislocation line per unit | J/m |
| $\sigma$ | Interfacial energy | J/m$^2$ |
| $\sigma_{M_i}$ | Specific interfacial energy between $M_iC$ and matrix | J/m$^2$ |
| $\Delta G_V$ | Volume free energy | J/m$^3$ |
| $\Delta G^*$ | Critical nuclear power in austenite | J |
| $\Delta G_d{}^*$ | Critical nuclear power in ferrite | J |
| $V_m$ | Molar volume of precipitates | m$^3$/mol |
| $A, B$ | Constants of precipitates in the solubility product formula | - |
| $n, x, y, z$ | Stoichiometric coefficient | - |
| $\eta$ | Shape factor | - |
| $Q$ | Activation energy for atoms | J/mol |
| $k$ | Boltzmann constant | - |

## 3. Results and Discussion

### 3.1. Quantitative Analysis of Precipitation in Ti-Mo and Ti−Mo−V Steels

In our previous works [13–16], it was found that the addition of V significantly improved the yield strength and tensile strength of Ti−Mo steel by ~28% and ~30%, respectively, mainly due to the increment of precipitation strengthening by (Ti, Mo, V)C precipitates. To further confirm the quantitative results of precipitates in Ti−Mo and Ti−Mo−V steels, electrolytically extracted phase analysis was carried out, and the results are shown in Tables 3 and 4. It can be found that the Ti is almost completely precipitated in the two experimental steels, and the precipitation of Mo in Ti−Mo and Ti−Mo−V steel is similar. Nevertheless, the volume fraction of MC precipitates increases from 0.242% to 0.389% by addition of V. The precipitation of M$_3$C is mainly controlled by the thermomechanical control process (TMCP) [14]. More C is consumed by forming MC particles in Ti−Mo−V steel, resulting in the mass fraction of M$_3$C in Ti−Mo−V steel, which is less than that in Ti−Mo steel (0.391% vs. 0.416%).

**Table 3.** Quantitative analysis of MC precipitates of Ti−Mo and Ti−Mo−V steel.

| Steel | Mass Fraction of Element in MC Phase/% | | | | | $f_v$/% |
|-------|------|------|------|------|------|--------|
| | Ti [a] | Mo | V | C [b] | $\sum$ | |
| Ti−Mo | 0.082 | 0.085 | - | 0.031 | 0.212 | 0.242 |
| Ti−Mo−V | 0.077 | 0.087 | 0.086 | 0.050 | 0.300 | 0.389 |

[a] Mass fraction of Ti in TiN was deducted. [b] Carbon content was an estimated result according to MC formula.

**Table 4.** Quantitative analysis of $M_3C$ precipitates of Ti−Mo and Ti−Mo−V steel.

| Steel | Mass Fraction of Element in $M_3C$ Phase/% | | | | | |
|---|---|---|---|---|---|---|
| | **Fe** | **Mn** | **Mo** | **V** | **C [c]** | **$\sum$** |
| Ti−Mo | 0.323 | 0.033 | 0.026 | - | 0.027 | 0.416 |
| Ti−Mo−V | 0.299 | 0.018 | 0.031 | 0.01 | 0.025 | 0.391 |

[c] Carbon content was an estimated result according to $M_3C$ formula.

### 3.2. Precipitation Characterization

To clarify the morphology and position of precipitates in the matrix, the TEM observation of Ti−Mo−V steel is shown in Figure 2. The results show that a large number of precipitates exist in the steel. Meanwhile, the coarse particles (over 50 nm) mainly present two types, as shown in Figure 2a. The first type is large ellipsoidal particles (P1) that precipitated in the ferrite grains, which is identified as Ti-enriched (Ti, Mo, V) C particles (Figure 2c). The second type (P2) is verified as cementite mainly distributed in the grain boundaries. According to the previous studies [18,19], these (Ti, Mo, V)C particles are mainly precipitated during the soaking at high temperature.
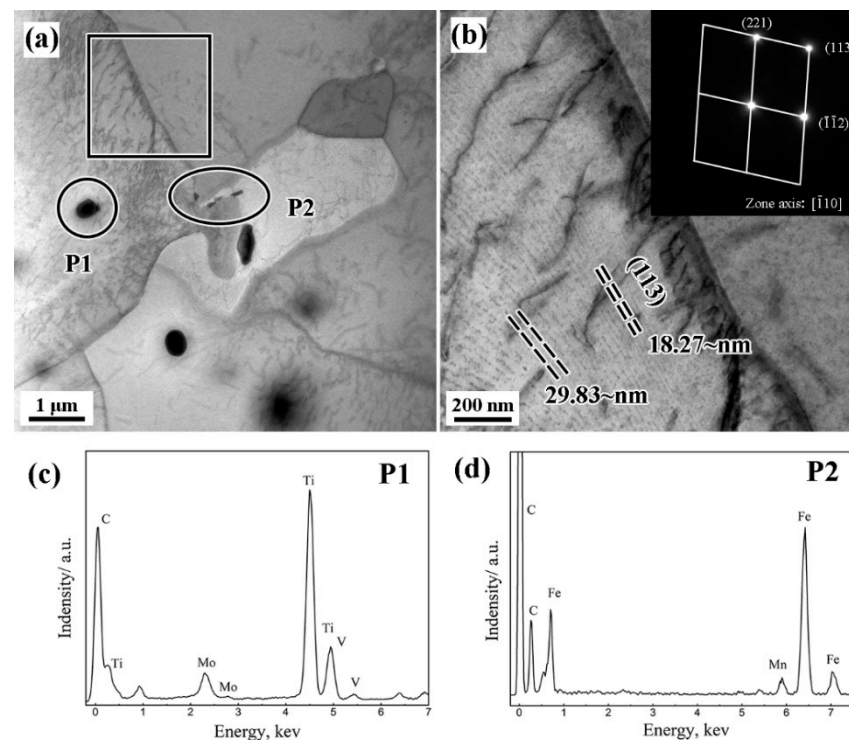


**Figure 2.** TEM and EDS images of particles in Ti−Mo−V steel. (**a**) TEM morphologies; (**b**) Interphase precipitation morphologies; (**c**) EDS analysis result of P1; (**d**) EDS analysis result of P2.

In addition, nano-sized interphase precipitation is also observed in Figure 2b. It can be found that the precipitation spacing and morphology of the interphase precipitates change with the distance from the grain boundary. Yan et al. [20] pointed that the spacing of interphase precipitation was mainly related to the movements of the $\gamma/\alpha$ interface during the phase transformation. At the distance from the grain boundary, corresponding to the early stage of ferrite transformation, the phase transformation driving force is larger, resulting in faster movement of the $\gamma/\alpha$ interface. At this stage, the mechanism of interphase precipitation is a bowing mechanism, which leads to the irregular and larger particle spacing of interphase precipitation [20,21]. At the later stage of phase transformation, the $\gamma/\alpha$ interface moves slowly due to the decrease of phase transformation driving force, thereby changing to the quasi-step mechanism of interphase precipitation [22].

Then, the morphology of interphase precipitation changes to regular particle spacing in the (113) crystal planes of ferrite, and the interphase precipitation spacing decreases from 29.83 nm to 18.27 nm.

Another type of nano-sized particles is randomly dispersed precipitates. These carbides tend to precipitate at high energy sites, such as grain boundaries and dislocations. The bright-field image, dark-field image and electronic diffraction pattern of precipitates were observed by using the thin foil sample of experimental steel, as shown in Figure 3. The results indicate that the orientation relationship between (Ti, Mo, V)C precipitates and the ferrite matrix is clarified as $(111)_{(Ti, Mo,V)C}//(01\bar{1})_{\alpha-Fe}$ and $[01\bar{1}]_{(Ti, Mo,V)C}//[\bar{1}11]_{\alpha-Fe}$ which agrees with the K−S relationship [14], and its lattice constant is calculated to be 0.423 nm. It means that these (Ti, Mo, V)C particles are mainly precipitated in the austenite during the rolling process. Meanwhile, the (Ti, Mo, V) C particles distributed in the trigeminal grain boundary can inhibit the movement of grain boundaries and refine the ferritic grains.
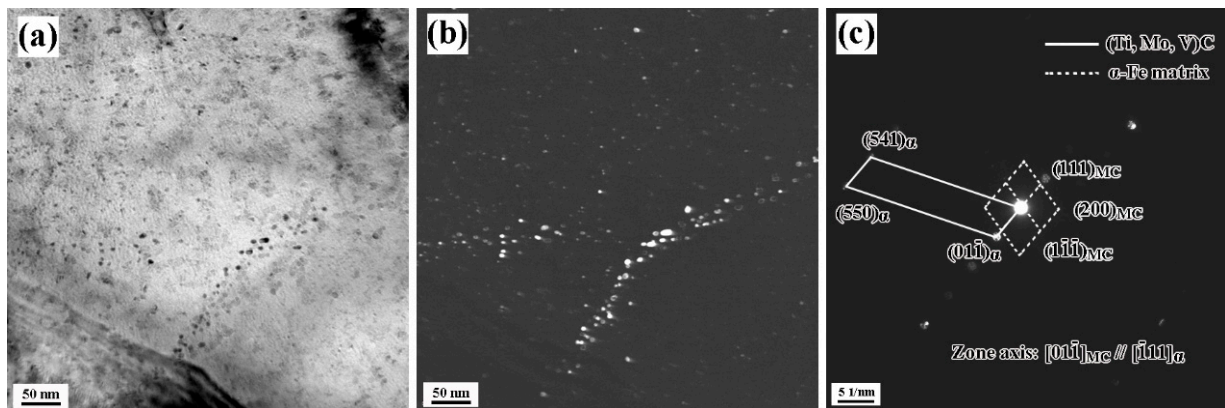


**Figure 3.** The (**a**) bright-field image (**b**), dark-field image of precipitates and (**c**) diffraction pattern of precipitates.

Figure 4 shows the Fourier transform of high-resolution image of precipitates with the size below 10 nm. It can be found that their orientation relationship agrees with the B−N relationship as $(200)_{(Ti, Mo,V)C}//(200)_{\alpha-Fe}$ and $[011]_{(Ti, Mo,V)C}//[001]_{\alpha-Fe}$ This indicates that these particles are precipitated in the ferrite, which can provide stronger precipitation strengthening.
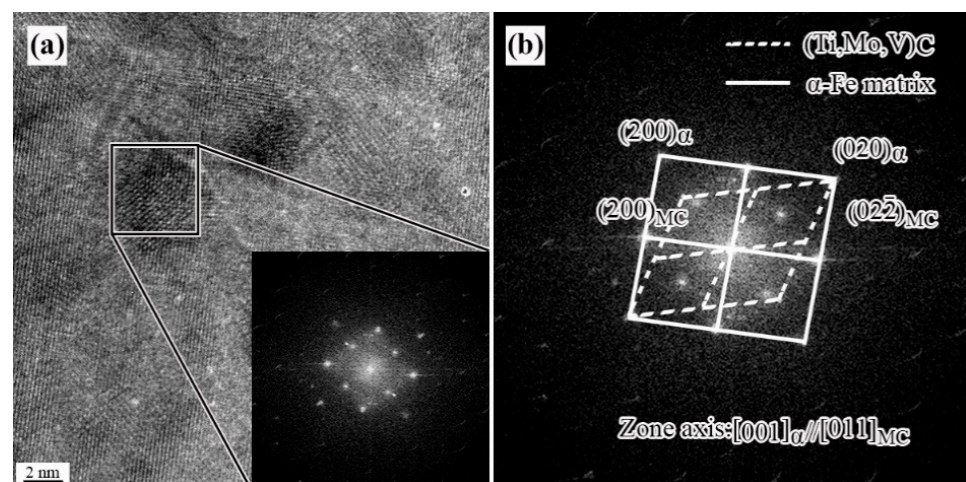


**Figure 4.** (**a**) High resolution TEM micrograph of the precipitation and (**b**) fast Fourier transformed.

### 3.3. Effect of V on the Precipitation Behavior in the Austenite of Ti−Mo Steel

According to the previous studies [23], the nano-sized carbides precipitated in the austenite refined the microstructure and strengthened the matrix. In addition, the precipitation behavior of carbides can be analyzed by thermodynamic and kinetic models [24]. It should be noted that the Ti easily forms TiN precipitates with lower solubility at a higher temperature. Additionally, the N in the experimental steel is an incidental element in the smelting. Thus, in order to facilitate the calculations, the N in experimental steel is assumed to be consumed completely, and the content of Ti in experimental steel is modified according to the stoichiometry of TiN in the relevant calculation. Furthermore, the content of the microalloying elements solid-solved in the austenite matrix at different temperatures can be calculated according to the solid solubility product formulae of TiC, MoC and VC.

Its formulae are as follows [14,15,24]

$$\lg\{[Ti] \cdot [C]\}_\gamma = 2.75 - 7000/T \tag{1}$$

$$\lg\{[Mo] \cdot [C]\}_\gamma = 4.251 - 3468/T \tag{2}$$

$$\lg\{[V] \cdot [C]\}_\gamma = 6.72 - 9500/T \tag{3}$$

$$f_v = \left(\sum M_i - \sum [M_i] + C - [C]\right)\frac{\rho_{Fe}}{100\rho_{MC}} \tag{4}$$

where the meanings and units of different symbols are shown in Table 2. The subscript $\gamma$ indicates that the formula is applicable to the austenite matrix. The TiC, MoC and VC in the steel are all NaCl-type face-centered cubic structures, which can be mutually solved with each other. Therefore, the chemical formulae of (Ti, Mo)C and (Ti, Mo, V)C can be expressed as $Ti_xMo_yC$ ($x + y = 1$) and $Ti_xMo_yV_zC$ ($x + y + z = 1$), respectively. Figure 5 shows the effects of temperature on the stoichiometric coefficient of $Ti_xMo_yC$ and $Ti_xMo_yV_zC$. The results show that the precipitates in Ti-Mo steel are mainly Ti-enriched (Ti, Mo)C, and the proportion of Ti is above 99.5%. For Ti−Mo−V steel, the precipitate is Ti-enriched (Ti, Mo, V)C at the higher temperature. However, with the decrease of temperature, the proportion of Ti in the (Ti, Mo, V)C decreases obviously, but the proportion of V increases. Meanwhile, the proportion of Mo is almost unchanged. This indicates that the Ti element has a high precipitation temperature, and the Mo element is basically not precipitated in austenite at high temperatures.
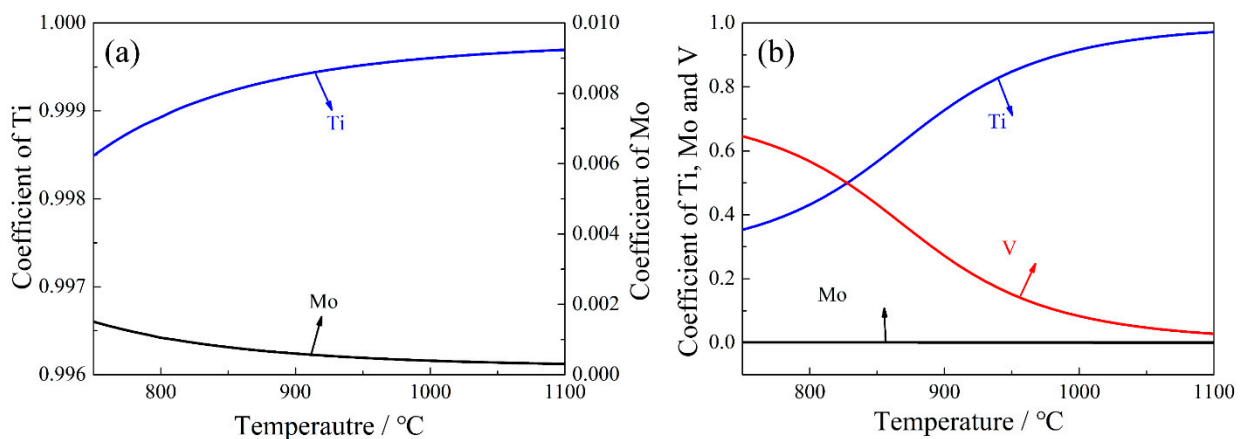


**Figure 5.** Effects of temperature on the formula coefficient of (**a**) $Ti_xMo_yC$ and (**b**) $Ti_xMo_yV_zC$ in austenite.

According to the thermodynamics calculation, the precipitation volume fractions of (Ti, Mo)C and (Ti, Mo, V)C as a function of temperature are obtained, as shown in Figure 6. The volume fraction of (Ti, Mo, V)C is significantly higher than that of (Ti, Mo)C and both of them increase with the decrease of temperature. When the temperature is lower than 900 °C, a

large amount of V is precipitated and the volume fraction of (Ti, Mo, V)C increases rapidly, resulting in a larger difference between the volume fractions of (Ti, Mo, V)C and (Ti, Mo)C.
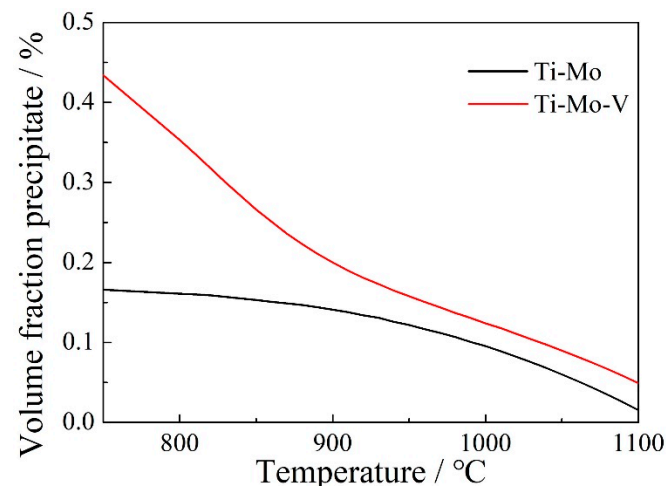


**Figure 6.** Volume fractions of precipitation in Ti−Mo and Ti−Mo−V steels as a function of temperature in austenite.

The kinetic model is based on the following assumptions: (1) MC particles nucleate on the dislocation line, and the nucleation rate rapidly decays to zero; (2) the edge dislocation is considered as the nucleation positions of precipitated particles; (3) the shape of precipitation is considered to spheroid. Then, the interfacial energy and driving force of (Ti, Mo)C and (Ti, Mo, V) can be expressed as [24–26]:

$$\sigma = \sum n \cdot \sigma_{M_i} \tag{5}$$

$$\Delta G_V = \frac{1}{V_{\mathrm{m}}}\left\{-19.1446B + 19.1446T\left[A - \log\left(\prod [M_i]^n [C]\right)\right]\right\} \tag{6}$$

where the meanings and units of different symbols are shown in Table 2. The nucleation rate and precipitation start time of precipitates in different temperatures can be calculated by Formulas (7) and (8), respectively [15,24–26].

$$I = K \cdot d^{*2} \cdot \exp\left(\frac{\Delta G^* + Q}{kT}\right) \tag{7}$$

$$\lg\left(\frac{t_{0.05da}}{t_{0da}}\right) = \left[-1.28994 - 2\lg d^*\left(\frac{1}{\ln 10} \times \frac{(1 + \frac{A\Delta G_V}{2\pi\sigma^2})\Delta G^* + \frac{5}{3}Q}{kT}\right)\right] \tag{8}$$

where the meanings and units of different symbols are shown in Table 2.

The curves of interfacial energy, Gibbs free energy, nucleation rate-temperature (NrT) and precipitated-time-temperature (PTT) of the precipitates in Ti−Mo and Ti−Mo−V steels are shown in Figure 7. The results indicate that the interfacial energy and driving force of (Ti, Mo)C and (Ti, Mo, V)C increases with the decrease of temperature. When the temperature is higher than 902 °C, the interfacial energy of (Ti, Mo, V)C is similar to that of (Ti, Mo)C, and the driving force of (Ti, Mo, V)C is higher than that of (Ti, Mo)C, resulting in the NrT and PTT curves of (Ti, Mo, V)C shifting toward the top zone. Moreover, when the temperature is lower than 902 °C, the driving force for (Ti, Mo, V)C is significantly lower than that for (Ti, Mo)C, but the interfacial energy of (Ti, Mo, V)C/austenite is lower than that of (Ti, Mo)C/austenite. Thus, combined with the influence of driving force and interfacial energy on the precipitation, the precipitation of (Ti, Mo, V)C can be promoted above 872 °C.
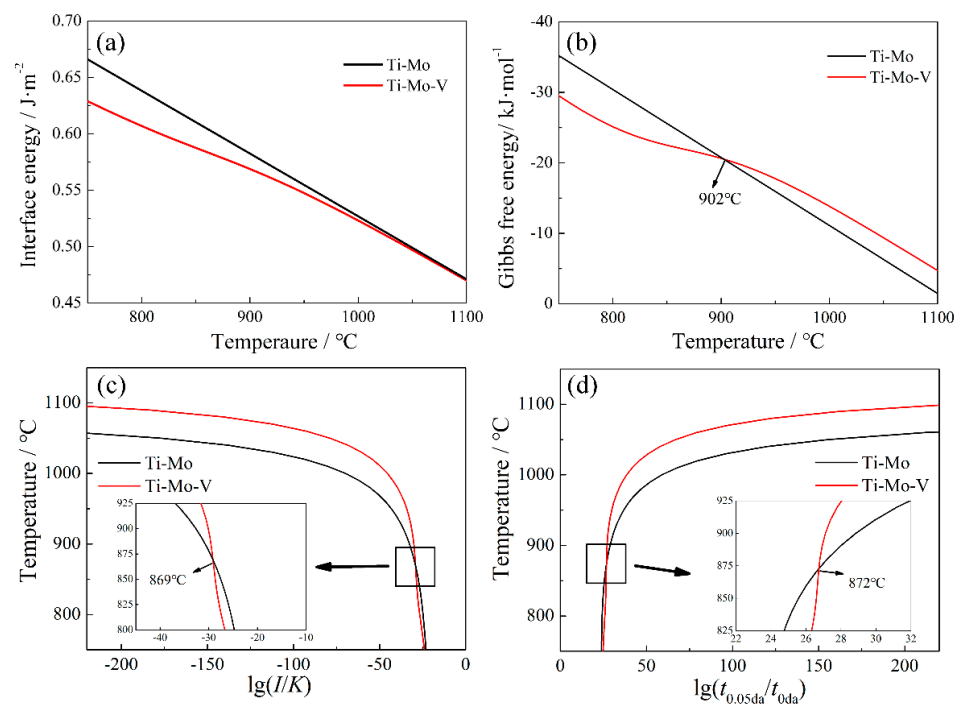
**Figure 7.** The kinetic analysis in austenite of Ti−Mo and Ti−Mo−V steels. (**a**) curve of interfacial energy, (**b**) curve of Gibbs free energy, (**c**) curve of NrT and (**d**) curve of PTT.

### 3.4. Effect of V on the Precipitation Behavior in Ferrite of Ti−Mo Steel

It is well-known that the microalloying elements solubility in ferrite are significantly lower than those in austenite. The supersaturated solute microalloying elements will further precipitate in the ferrite during the coiling process. Compared to austenite, the precipitation precipitated in ferrite is smaller in size, thereby producing stronger precipitation strengthening [18,19,26]. It should be noted that the contents of solid solution of microalloying elements and carbon in the austenite at 860 °C are used as the initial content in the ferrite calculation model. The solution product formulas of TiC, MoC and VC in ferrite are as follows [18,19,27–29]:

$$\lg\{[Ti]\cdot[C]\}_\alpha = 4.4 - 9575/T \tag{9}$$

$$\lg\{[Mo]\cdot[C]\}_\alpha = 6.163 - 7583/T \tag{10}$$

$$\lg\{[V]\cdot[C]\}_\alpha = 4.55 - 8300/T \tag{11}$$

where the meanings and units of different symbols are shown in the Table 2. The subscript $\alpha$ indicates that the formula is applicable to the ferrite matrix. Figure 8 shows the stoichiometric coefficient of $Ti_xMo_yC$ and $Ti_xMo_yV_zC$ as a function of temperature in ferrite. The results show that as the temperature decreases, the proportion of Ti content decreases rapidly, whereas the proportion of Mo content increases. The precipitates in ferrite are Mo-enriched (Ti, Mo)C. For (Ti, Mo, V)C; with the decreases of temperature, the proportion of V decreases, but the proportion of Mo increases, whereas the proportion of Ti is basically unchanged. Meanwhile, the precipitation in the steel is mainly V-enriched (Ti, Mo, V)C particles, and the proportion of V content was above 85%. This indicates that V is the dominant element of (Ti, Mo, V)C in ferrite.
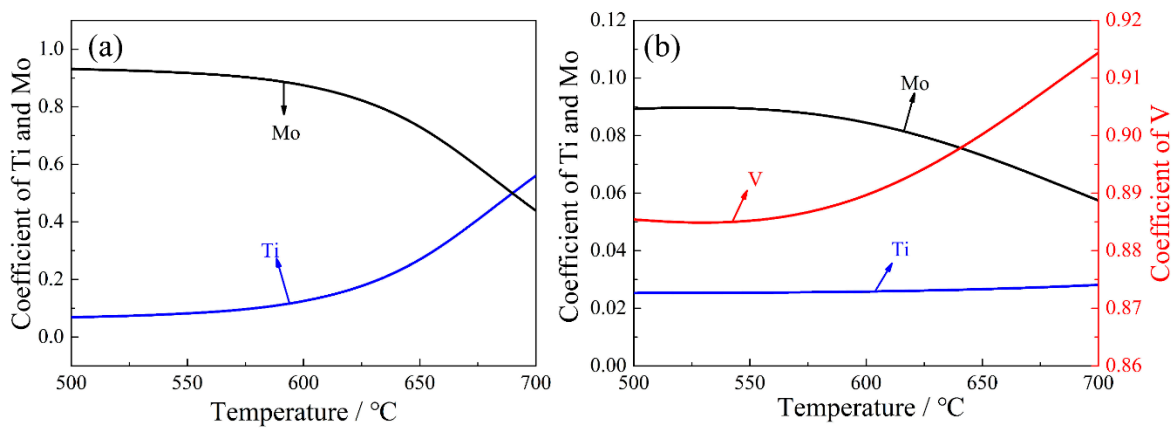
**Figure 8.** The formula coefficient of (**a**) Ti$_x$Mo$_y$C and (**b**) Ti$_x$Mo$_y$V$_z$C in ferrite as a function of temperature.

Figure 9 is the curve of the volume fraction of precipitation in ferrite with temperature. The results indicate that the volume fraction of precipitates increases with the decrease of temperature. The precipitation of V leads to the fact that the volume fraction of (Ti, Mo, V)C in ferrite is significantly higher than that of (Ti, Mo)C.
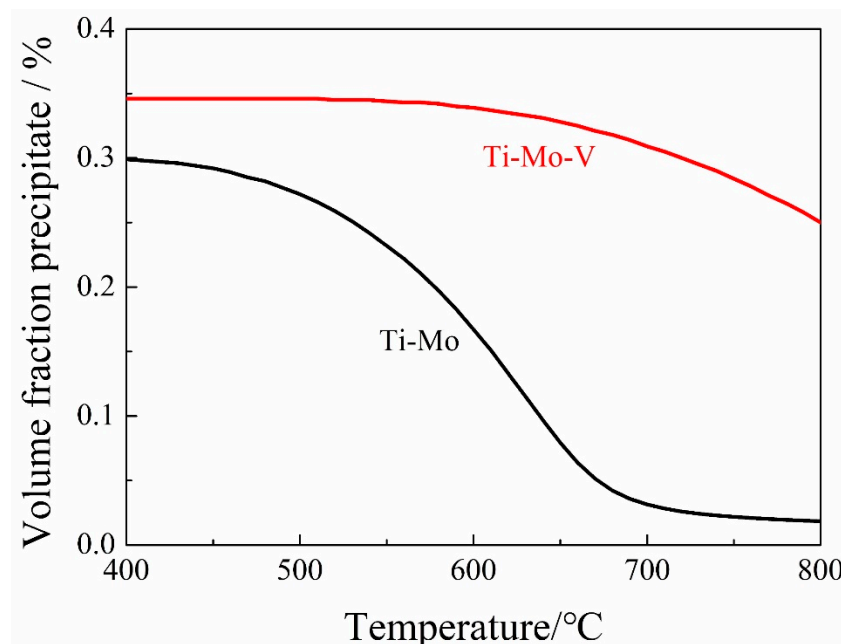


**Figure 9.** Volume fractions of precipitation in Ti−Mo and Ti−Mo−V steels as a function of temperature in ferrite.

Different from austenite, the precipitates in ferrite mainly present rod-like and disc-like, and the orientation relationship between precipitation and ferritic matrix changes from a K−S relationship to a B−N relationship. The kinetic model in ferrite needs to introduce shape factors $\eta$, whereas $d^*$ and $\Delta G^*$ are transformed into $d_d^*$ and $\Delta G_d^*$. Therefore, Equations (7) and (8) have been changed to Equations (12) and (13), respectively [24–26].

$$I = K \cdot d_d^{*2} \cdot \exp\left(\frac{\Delta G_e^* + Q}{kT}\right) \tag{12}$$

$$\lg\left(\frac{t_{0.05da}}{t_{0da}}\right) = \left[-1.28994 - 2\lg d_d^*\left(\frac{1}{\ln 10} \times \frac{(1 + \frac{\eta A \Delta G_V}{2\pi\sigma^2})\Delta G_e^* + \frac{5}{3}Q}{kT}\right)\right] \tag{13}$$

where the meanings and units of different symbols are shown in Table 2.

Figure 10 presents the interfacial energy, Gibbs free energy, NrT and PTT curves of (Ti, Mo)C and (Ti, Mo, V)C precipitated in the ferrite. It is found that PTT curve of (Ti, Mo, V)C precipitated in the ferrite region is "C" shaped, but that of (Ti, Mo)C is "ε" shaped. The driving force for (Ti, Mo, V)C is higher than that for (Ti, Mo)C, and the interfacial energy of (Ti, Mo, V)C/ferrite is lower than that of (Ti, Mo)C/ferrite, resulting in the nucleation rate of (Ti, Mo, V)C in ferrite being significantly larger than that of (Ti, Mo)C. Consequently, the precipitation of (Ti, Mo, V)C in ferrite is greatly promoted, and improved the precipitation strengthening of Ti−Mo−V hot-rolled ferritic steel.
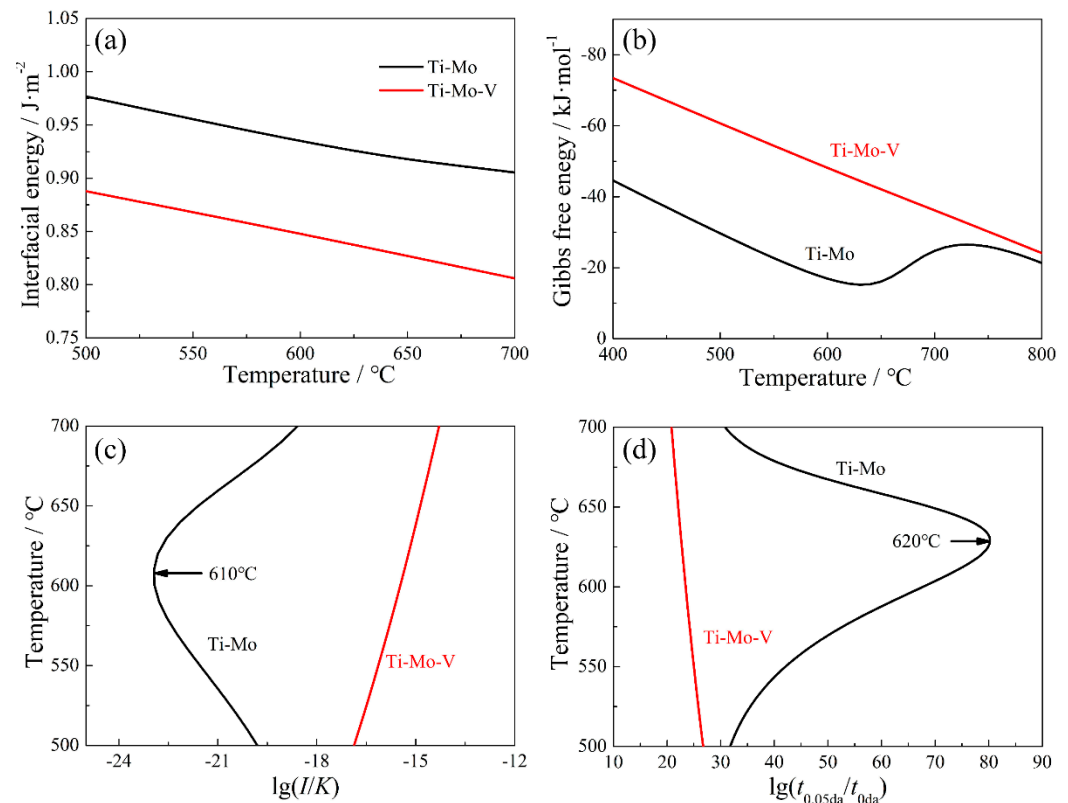


**Figure 10.** The thermodynamic and kinetic analysis in ferrite of Ti−Mo and Ti−Mo−V steels. (**a**) curve of interfacial energy, (**b**) curve of Gibbs free energy, (**c**) curve of NrT and (**d**) curve of PTT.

## 4. Conclusions

In this study, the precipitates of Ti−Mo−V microalloyed high-strength steel were characterized in detail. The effect of V addition on precipitation behavior in austenite and ferrite was explored. The main conclusion could be summarized as follows:

1.  The addition of V can significantly increase the volume fraction of the (Ti, Mo, V)C precipitates in Ti−Mo−V steel (0.242% vs. 0.389%). The precipitation characterization shows that the (Ti, Mo, V)C particles can be divided into three types: spherical precipitates in austenite after deformation, interphase precipitates during $\gamma \rightarrow \alpha$ transformation and dispersive nano-sized precipitates in the supersaturated ferrite matrix.

2.  The results of theoretical calculation indicate that when the temperature is higher than 872 °C, the addition of vanadium can increase the driving force for (Ti, Mo, V)C precipitation in austenite, resulting in an increased nucleation rate and shortened incubation period, promoting the (Ti, Mo, V)C precipitation.

3.  The PTT curve of (Ti, Mo, V)C precipitated in the ferrite region is "C" shaped, but that of (Ti, Mo)C is "ε" shaped, and the incubation period of (Ti, Mo, V)C is significantly shorter than that of (Ti, Mo)C.

## References

1. Song, R.; Fonstein, N.; Jun, H.J.; Pottore, N.; Bhattacharya, D.; Jansto, S. Effects of Nb on Microstructural Evolution and Mechanical Properties of Low-Carbon Cold-Rolled Dual-Phase Steels. *Metallogr. Microstruct. Anal.* **2014**, *3*, 174–184. [CrossRef]
2. Hu, J.; Du, L.X.; Ma, Y.N.; Guo, G.S.; Xie, H.; Mirsa, R.D.K. Effect of microalloying with molybdenum and boron on the microstructure and mechanical properties of ultra-low-C Ti bearing steel. *Mater. Sci. Eng. A* **2015**, *640*, 259–266. [CrossRef]
3. Liu, C.; Xiong, F.; Wang, Y.; Cao, Y.; Liu, X.; Xue, Z.; Peng, Q.; Peng, L. Strengthening Mechanism and Carbide Precipitation Behavior of Nb-Mo Microalloy Medium Mn Steel. *Materials* **2021**, *14*, 7461. [CrossRef] [PubMed]
4. Yuan, J.; Xiao, Y.; Min, N.; Li, W.; Zhao, S. The Influence of Precipitate Morphology on the Growth of Austenite Grain in Nb-Ti-Al Microalloyed Steels. *Materials* **2022**, *15*, 3176. [CrossRef] [PubMed]
5. Li, X.; Yang, J.; Li, Y.; Liu, L.; Jin, C.; Gao, X.; Deng, X.; Wang, Z. A Systematical Evaluation of the Crystallographic Orientation Relationship between MC Precipitates and Ferrite Matrix in HSLA Steels. *Materials* **2022**, *15*, 3967. [CrossRef]
6. Saito, N.; Fukahori, M.; Minote, T.; Funakawa, Y.; Hisano, D.; Hamasaki, H.; Yoshida, F. Elasto-viscoplastic behavior of 980 MPa nano-precipitation strengthened steel sheet at elevated temperatures and spring back in warm bending. *Int. J. Mech. Sci.* **2018**, *146–147*, 571–582. [CrossRef]
7. Timokhina, I.; Miller, M.K.; Wang, J.; Beladi, H.; Cizek, P.; Hodgson, P.D. On the Ti-Mo-Fe-C atomic clustering during interphase precipitation in the Ti-Mo steel studied by advanced microscopic techniques. *Mater. Des.* **2016**, *111*, 222–229. [CrossRef]
8. Huang, Y.; Liu, W.; Zhao, A.; Han, J.; Wang, Z.; Yin, H. Effect of Mo content on the thermal stability of Ti-Mo-bearing ferritic steel. *Int. J. Miner. Metall. Mater.* **2021**, *28*, 412–421. [CrossRef]
9. Funakawa, Y.; Shiozaki, T.; Tomita, K.; Yamamoto, T.; Maeda, E. Development of High Strength Hot-rolled Sheet Steel Consisting of Ferrite and Nanometer-sized Carbides. *ISIJ Int.* **2004**, *44*, 1945–1951. [CrossRef]
10. Cai, M.; Chen, L.; Fang, K.; Huang, H.; Hodgson, P. The effects of a ferritic or martensitic matrix on the tensile behavior of a nano-precipitation strengthened ultra-low carbon Ti–Mo–Nb steel. *Mater. Sci. Eng. A* **2021**, *801*, 140410. [CrossRef]
11. Bu, F.Z.; Wang, X.M.; Chen, L.; Yang, S.W.; Shang, C.J.; Misra, R.D.K. Influence of cooling rate on the precipitation behavior in Ti–Nb–Mo microalloyed steels during continuous cooling and relationship to strength. *Mater. Charact.* **2015**, *102*, 146–155. [CrossRef]
12. Huang, H.; Yang, G.; Zhao, G.; Mao, X.; Gan, X.; Yin, Q.; Yi, H. Effect of Nb on the microstructure and properties of Ti-Mo microalloyed high-strength ferritic steel. *Mater. Sci. Eng. A* **2018**, *736*, 148–155. [CrossRef]
13. He, X.; Yang, G.; Mao, X.; Yu, C.; Da, C.; Gan, X. Effect of Nb on the Continuous Cooling Transformation Rule and Microstructure, Mechanical Properties of Ti-Mo Bearing Microalloyed Steel. *Acta Metall. Sin.* **2017**, *53*, 648–656.
14. Gan, X.L.; Yang, G.W.; Zhao, G.; Mao, X.P.; Huang, H.H.; Xu, G. Effect of Vanadium on the Phase Transformation Behavior of Ti–Mo Microalloyed Ultra-High Strength Steel. *Steel Res. Int.* **2018**, *89*, 1800112.
15. Zhang, K.; Li, Z.D.; Sun, X.J.; Yong, Q.L.; Yang, J.W.; Li, Y.M.; Zhao, P.L. Development of Ti–V–Mo Complex Microalloyed Hot-Rolled 900-MPa-Grade High-Strength Steel. *Acta Metall. Sin. Engl. Lett.* **2015**, *28*, 641–648. [CrossRef]
16. Fu, Z.; Yang, G.; Han, R.; Xu, Y.; Mao, X.; Bao, S.; Zhao, G. Influence of coiling temperature on microstructure and mechanical properties of a hot-rolled high-strength steel microalloyed with Ti, Mo and V. *J. Iron Steel Res. Int.* **2022**, *29*, 10. [CrossRef]
17. Yang, G.; Sun, X.; Li, Z.; Li, X.; Yong, Q. Effects of vanadium on the microstructure and mechanical properties of a high strength low alloy martensite steel. *Mater. Des.* **2013**, *50*, 102–107. [CrossRef]
18. Xu, L.; Wu, H.; Tang, Q. Effects of Coiling Temperature on Microstructure and Precipitation Behavior in Nb–Ti Microalloyed Steels. *ISIJ Int.* **2018**, *58*, 1086–1093. [CrossRef]
19. Misra, R.D.K.; Nathani, H.; Hartmann, J.E.; Siciliano, F. Microstructural evolution in a new 770MPa hot rolled Nb–Ti microalloyed steel. *Mater. Sci. Eng. A* **2005**, *394*, 339–352. [CrossRef]
20. Yen, H.; Chen, P.; Huang, C.; Yang, J. Interphase precipitation of nanometer-sized carbides in a titanium–molybdenum-bearing low-carbon steel. *Acta Mater.* **2011**, *59*, 6264–6274. [CrossRef]
21. Ricks, R.A.; Howell, P.R. The formation of discrete precipitate dispersions on mobile interphase boundaries in iron-base alloys. *Acta Mater.* **1983**, *31*, 853–861. [CrossRef]
22. Gong, P.; Liu, X.G.; Rijkenberg, A.; Rainforth, W.M. The effect of molybdenum on interphase precipitation and microstructures in microalloyed steels containing titanium and vanadium. *Acta Mater.* **2018**, *161*, 374–387. [CrossRef]

23. Park, D.; Huh, M.; Shim, J.; Suh, J.; Lee, K.; Jung, W. Strengthening mechanism of hot rolled Ti and Nb microalloyed HSLA steels containing Mo and W with various coiling temperature. *Mater. Sci. Eng. A* **2013**, *560*, 528–534. [CrossRef]

24. Yong, Q.L. *Secondary Phases in Steels*; Metallurgy Industry Press: Beijing, China, 2006.

25. Chen, S.; Li, L.; Peng, Z.; Huo, X.; Gao, J. Strain-induced precipitation in Ti microalloyed steel by two-stage controlled rolling process. *J. Mater. Res. Technol.* **2020**, *9*, 15759–15770. [CrossRef]

26. Zhang, K.; Sun, X.-J.; Li, Z.-D.; Xu, K.; Jia, T.; Zhu, Z.-H.; Ye, X.-Y.; Kang, J.-Y.; Yong, Q.-L. Effect of ti/v ratio on thermodynamics and kinetics of mc in $\gamma/\alpha$ matrices of ti-v microalloyed steels. *J. Iron Steel Res. Int.* **2021**, *28*, 1019–1029. [CrossRef]

27. Kim, Y.W.; Hong, S.; Huh, Y.; Lee, C.S. Role of rolling temperature in the precipitation hardening characteristics of Ti–Mo microalloyed hot-rolled high strength steel. *Mater. Sci. Eng. A* **2014**, *615*, 255–261. [CrossRef]

28. Kim, Y.W.; Kim, J.H.; Hong, S.; Lee, C.S. Effects of rolling temperature on the microstructure and mechanical properties of Ti–Mo microalloyed hot-rolled high strength steel. *Mater. Sci. Eng. A* **2014**, *605*, 244–252. [CrossRef]

29. Taylor, K.A. Solubility products for titanium-, vanadium-, and niobium-carbide in ferrite. *Scr. Mater.* **1995**, *32*, 7–12. [CrossRef]